0D, 1D, 2D, and 3D simulations of an idealized coaxial impedance-matched Marx generator

D. V. Rose,[1,2] W. A. Stygar,[3] D. T. Offermann,[1] K. R. LeChien,[2,3] M. G. Anderson,[3] K. S. Raman,[3] A. E. Schmidt,[3] D. A. Max,[4] C. B. Beatty,[3] R. M. Anaya,[3] A. S. Anquillano,[5] A. Arsenlis,[3] A. M. Benson,[5] R. E. Beverly,[6] K. J. Boehm,[5] R. S. Chaffee,[3] J. E. Cortes,[3] W. A. Drews,[5] J. J. Edwards,[3] J. L. Ellsworth,[3] A. K. Gaikwad,[7] T. C. Genoni,[1] G. P. Grim,[3] K. T. Hadley,[3] J. H. Hammer,[3] M. C. Herrmann,[3] F. A. Howland,[2,3] T. M. Hutchinson,[3] J. B. Javedani,[3] A. J. Johnson,[3] B. J. Kelsall,[8] A. J. Link,[2,3] N. B. Meezan,[2,3] C. A. Mostrom,[1] C. B. Mostrom,[1] D. B. Norton,[3] I. Paraschiv,[1] A. M. Russell,[1] E. B. Smith,[3] N. C. Soni,[7] R. D. Speer,[3] R. B. Spielman,[9] C. H. Thoma,[1] R. P. Town,[3] J. J. Trueblood,[3] K. K. Tummel,[3] E. D. Watson,[1] J. A. Watson,[3] D. R. Welch,[1] A. D. White,[3] A. J. Young,[3] and A. B. Zylstra[2,3]

[1]*Voss Scientific, Albuquerque, New Mexico 87108, USA*
[2]*Pacific Fusion, Fremont, California 94538, USA*
[3]*Lawrence Livermore National Laboratory, Livermore, California 94550, USA*
[4]*Mission Support and Test Services, North Las Vegas, Nevada 89030, USA*
[5]*General Atomics Energy Group, San Diego, California 92121, USA*
[6]*R. E. Beverly III and Associates, Lewis Center, Ohio 43035, USA*
[7]*CSI Technologies, Vista, California 92081, USA*
[8]*MuEpsln, Chadds Ford, Pennsylvania 19317, USA*
[9]*Laboratory for Laser Energetics, U. of Rochester, Rochester, New York 14623, USA*

(Received 10 June 2024; accepted 22 October 2024; published 12 December 2024)

We have conducted 0D, 1D, 2D, and 3D simulations of an idealized coaxial impedance-matched Marx generator (IMG) [Phys. Rev. Accel. Beams **20**, 040402 (2017)]. The 0D calculations were conducted with a four-element circuit model; the 1D, 2D, and 3D calculations were conducted with highly resolved, fully electromagnetic representations. The IMG consists of 30 stages distributed axially and connected electrically in series. Each stage is powered by two bricks separated by 180° and connected electrically in parallel. Each brick comprises two opposite-polarity capacitors in series with a single switch. The bricks drive an internal impedance-matched coaxial transmission line terminated by a resistive load. The simulations neglect effects due to the switch-triggering circuit, the capacitor-charging circuit, external conducting boundaries, and reactive components of the load. We find dimensionality does not significantly affect the electrical power delivered by the IMG to its load: peak load powers estimated by the 0D, 1D, 2D, and 3D simulations agree to within 1%. The 3D calculations demonstrate that electromagnetic power radiated by the bricks, and axial gaps between stages, reduces the peak load power by less than ∼1%. Each simulation assumes the load impedance is 34% above that at which the load power is maximized. Operating an IMG with such an overmatched load offers several advantages while decreasing the peak load power by only 2%. The 0D, 1D, 2D, and 3D models outlined herein could be adapted to assess computationally competing IMG designs, and conduct a variety of numerical IMG experiments, *before* an IMG is constructed.

DOI: 10.1103/PhysRevAccelBeams.27.120401

I. INTRODUCTION

A Marx generator is an electrical circuit that charges capacitors in parallel and discharges them in series [1,2]. The *conventional* Marx was invented in 1924 by Erwin Marx [1]. Such a Marx is usually modeled with 0D circuit elements, and is designed to stack *voltages*.

The *impedance-matched* Marx generator (IMG) was invented in 2017 [3–20]. Like a conventional Marx, an IMG charges capacitors in parallel and discharges them in series. However, an IMG is designed to account for electromagnetic-wave propagation: an IMG is usually modeled with 1D transmission-line-circuit elements, and is designed to stack *waves*. As demonstrated by Ref. [3], all

Published by the American Physical Society under the terms of the Creative Commons Attribution 4.0 International license. Further distribution of this work must maintain attribution to the author(s) and the published article's title, journal citation, and DOI.

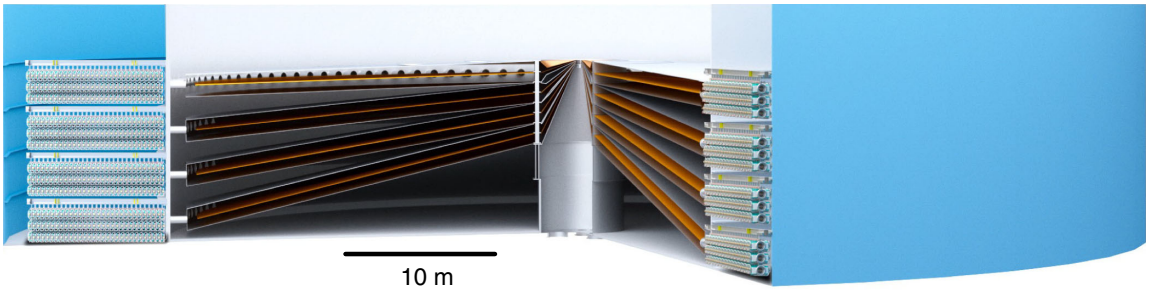


FIG. 1. Conceptual design of a next-generation pulsed-power accelerator. The 76-m-diameter machine is powered by 1440 IMGs. These are located in 120 towers distributed azimuthally around the accelerator; each tower consists of 12 IMGs arranged in a vertical stack. Each IMG includes 30 stages distributed axially and connected electrically in series. A single 30-stage IMG is illustrated by Fig. 2. The 1440 IMGs directly generate a 700-TW electromagnetic power pulse from dc-charged capacitors in a single step; the power is then delivered by transmission lines to the physics load. The load is located at the center of the accelerator, near the top of its centrally located vacuum section. The accelerator concept illustrated here delivers 90 MA to the load.

the reflected waves within an IMG cancel; all that is left are the forward-going waves. An IMG achieves electromagnetic-power amplification by triggered emission of radiation, and is a pulsed-power analog of a laser [3].

The IMG is an attractive candidate prime-power source for next-generation pulsed-power accelerators [21–26]. Like the linear transformer driver (LTD) [27–48], the IMG offers single-stage electrical pulse compression and impedance matching. In contrast to the LTD, the IMG is less expensive, less massive, and able to achieve slightly higher energy and power efficiencies due to the absence of ferromagnetic cores [3].

An IMG consists of a single stage or several stages distributed axially and connected electrically in series. Each stage is powered by a single brick or several bricks distributed azimuthally around the stage and connected electrically in parallel. Each brick comprises two opposite-polarity capacitors connected in series with a single switch located between the capacitors [29]. The stages of an IMG drive an impedance-matched transmission line. The simplest form of an IMG is a single brick that drives an impedance-matched load [3,21–24].

References [10,13] describe a prototype four-stage IMG that delivers a peak electrical power of 60 GW to a resistive load. Each stage is powered by two bricks located 180° apart. The IMG's eight bricks drive an internal impedance-matched coaxial transmission line terminated by the load. As indicated by Refs. [10,13], the measured load-power time history is consistent (within experimental uncertainties) with circuit simulations. Reference [19] describes the design and performance of a 330-GW IMG, which also performs as expected.

Figure 1 illustrates a conceptual design of a next-generation 700-TW pulsed-power accelerator that would deliver 90 MA to a physics load [10,13]. The design, which is under development, is powered by 1440 IMGs. The design assumes each IMG is a straightforward linear 30-stage extension of the four-stage prototype [10,13].

The 30-stage IMG concept is illustrated by Fig. 2. To establish a theoretical basis for its design, we have constructed three *virtual* IMGs: 1D, 2D, and 3D time-domain electromagnetic models of the 30-stage configuration. We used the models to simulate the IMG's electromagnetic performance; such simulations reduce risks associated with extrapolation of the four-stage prototype to the more powerful 30-stage module. The simulations assume an *idealized* IMG with an internal impedance-matched *coaxial* transmission line. The simulations neglect effects due to the switch-triggering circuit, the capacitor-charging circuit, external conducting boundaries, and reactive components of the load.

The 1D simulations were conducted with two 1D time-domain electromagnetic models of the 30-stage IMG. Each of the 1D models is a detailed transmission-line-circuit model that was constructed with CHICAGO-CIRCUITS, a transmission-line-circuit code [49]. The two 1D models and associated simulation results are presented by Sec. II.

The 2D simulations were conducted with two 2D finite-difference time-domain electromagnetic models of the 30-stage IMG. Each of the 2D models is powered by 30 identical transmission-line circuits; each circuit represents two bricks connected electrically in parallel. The two-brick circuit models were constructed with CHICAGO-CIRCUITS [49]. The 2D finite-difference regions of the 2D IMG models were constructed with CHICAGO, a finite-difference time-domain electromagnetic particle-in-cell code [50]. The 2D models, associated simulation results, and comparisons of 1D and 2D results are presented by Sec. III.

The 3D simulations were conducted with a 3D finite-difference time-domain electromagnetic model of the 30-stage IMG. The 3D model is not powered by external transmission-line circuits; instead, the model includes a 3D finite-difference time-domain electromagnetic model of each of the 60 bricks of the IMG. The 3D IMG model was constructed with the CHICAGO code [50]. The 3D model, associated simulation results, and a comparison of

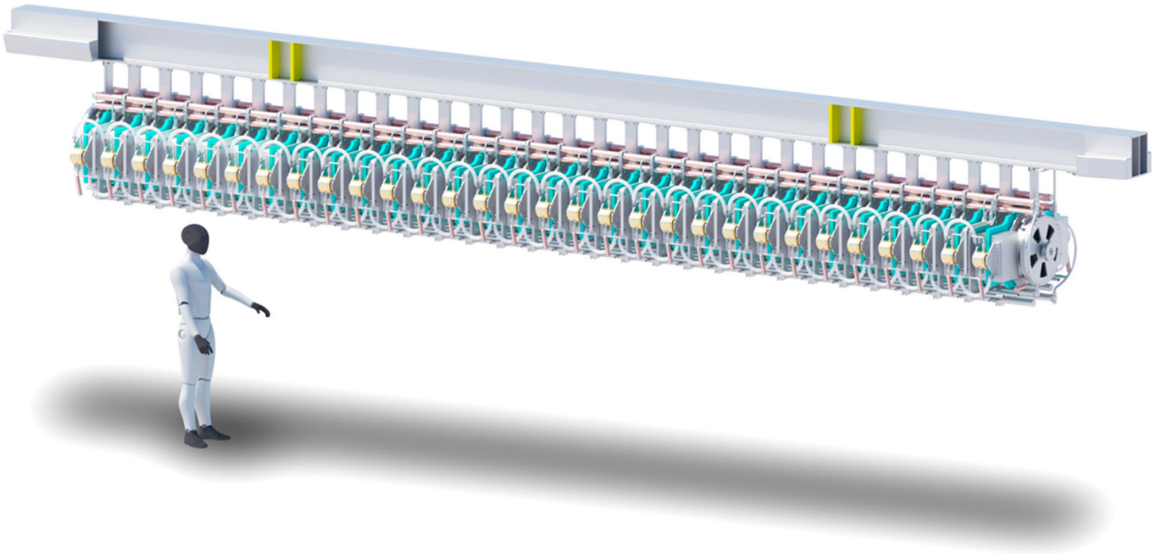


FIG. 2. Conceptual design of the 30-stage IMG. The stages are distributed axially and connected electrically in series. Each stage is powered by two bricks separated by 180° and connected electrically in parallel. Each brick comprises two opposite-polarity capacitors in series with a single three-electrode field-distortion gas switch. The bricks drive an internal impedance-matched coaxial transmission line.

1D, 2D, and 3D results are presented by Sec. IV. The 3D model is used to quantify electromagnetic power lost by the IMG due to electromagnetic radiation; results are also presented by Sec. IV.

The simulations described by this article assume the IMG-load impedance is 34% above that at which the peak electrical power delivered by the IMG to its load is maximized. The higher impedance reduces the peak load power by 2%; however, it is clear peak power is not the only IMG parameter of interest. As demonstrated by Sec. V, the higher load impedance offers several electrical-performance advantages.

Section VI summarizes the principal results of the article, and includes a discussion of proposed future work that would further refine and extend the modeling effort outlined herein. For completeness, the Appendix describes a 0D circuit model of the IMG. Numbered equations are in SI units throughout.

II. 1D ELECTROMAGNETIC MODELS

We have developed two 1D time-domain electromagnetic models of the IMG illustrated by Fig. 2. One model assumes the IMG's internal coaxial transmission line has a 10-step cathode; the other, a 30-step cathode. Each model is a detailed transmission-line-circuit model that was constructed with the CHICAGO-CIRCUITS code [49]. Each model comprises 500 transmission-line-circuit elements. The model of the 30-step-cathode IMG, which is the baseline design, is illustrated by Fig. 3.

As suggested by Figs. 2 and 3, each IMG considered by this article consists of 30 stages distributed axially and connected electrically in series. Each stage is powered by two bricks separated by 180° and connected electrically in parallel. Hence each IMG is powered by 60 bricks altogether.

Each of the 60 bricks is identical to every other brick. Each brick comprises two 100-kV 159.9-nF capacitors

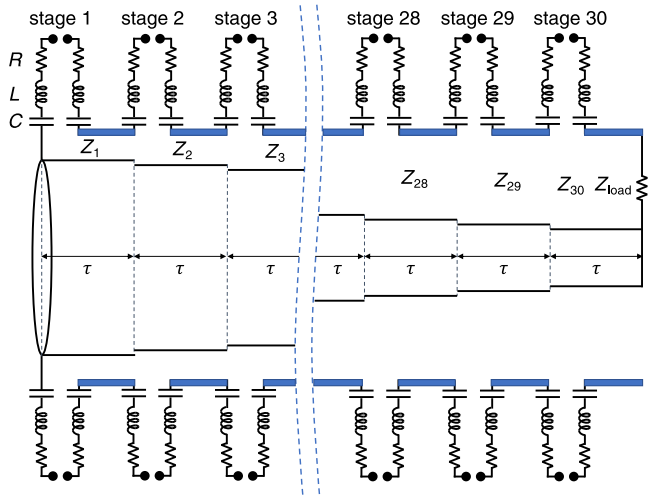


FIG. 3. Transmission-line-circuit model of the 30-stage IMG. The model assumes the inner (cathode) conductor of the IMG's internal impedance-matched coaxial transmission line has 30 steps. The model is constructed with 1D transmission-line-circuit elements. Stages 1 through 3, and 28 through 30, are represented here; stages 4 through 27 have been omitted. The impedance Z_j of the transmission-line segment associated with the jth stage is given by jZ_1, where $Z_1 = 1.117\ \Omega$. The model assumes $R = 0.035\ \Omega$, $L = 86$ nH, $C = 159.9$ nF, $\tau = 1.51$ ns, and $Z_{30} = Z_{\text{load}} = 33.514\ \Omega$.

connected electrically in series with a single (normally open) three-electrode field-distortion gas switch [10,13]. The switch is located between the two capacitors. The capacitors are dc charged to opposite polarities: one capacitor is charged to 100 kV; the other, −100 kV. Before the switch is triggered, a dc potential difference of 200 kV appears across the switch in a symmetric manner, so that one of the switch's two main electrodes is at 100 kV; the other, −100 kV.

The transmission-line-circuit model of a brick assumes the total series brick resistance is the sum of constant and time-dependent components. The constant component has a value of $2R$, as suggested by Fig. 3. The time-dependent component falls exponentially with time (with a 0.01-ns time constant) from an initially high value ($\sim 10^5$ Ω). The sum of the two components represents the sum of the following: switch resistance, equivalent series resistances of the brick's two capacitors, contact resistances throughout the brick, etc. A switch is triggered computationally by turning on the time-dependent component.

The model assumes the values of R, L, and C for the circuit elements illustrated by Fig. 3 are as follows:

$$R = 0.035\ \Omega, \tag{1}$$

$$L = 86\ \text{nH}, \tag{2}$$

$$C = 159.9\ \text{nF}. \tag{3}$$

As suggested by Fig. 3, the quantity L is one-half the total brick inductance, and C is the capacitance of each of the two brick capacitors.

When we constructed the 3D numerical model of the IMG described by Sec. IV, we intended the capacitance of each capacitor to be 160 nF. (An IMG powered by 160-nF capacitors generates an electromagnetic power pulse with a ∼100 ns rise time, which is approximately that required to drive many experiments of interest.) Subsequent 3D simulations determined that the actual value of the capacitance in the 3D model is 159.9 nF. To maintain consistency, this value is assumed by all the simulations throughout the article. The values for R and L listed above are also obtained from the 3D model and used throughout.

As suggested by Fig. 3, the 60 bricks drive an internal impedance-matched coaxial transmission line. For the baseline IMG, the 1D model assumes the transmission line's inner (cathode) conductor has 30 steps, one per stage, as illustrated by Fig. 3. The impedance of the coaxial-transmission-line segment associated with the jth stage is given by the following expression:

$$Z_j = jZ_1 \quad \text{for } j = 1, 2, \ldots, 30, \tag{4}$$

where

$$Z_1 = 1.117\ \Omega. \tag{5}$$

For the reasons discussed by Sec. V, Z_1 is 34% above the load impedance at which the peak electromagnetic power generated by each IMG brick (and hence the peak power delivered by the IMG to its load) is maximized. The model assumes the 30-step coaxial transmission line is terminated by a load with a pure resistance Z_{load}:

$$Z_{30} = Z_{\text{load}} = 33.514\ \Omega. \tag{6}$$

As indicated by Fig. 3, the 1D circuit model assumes the one-way transit time of each of the 30 segments of the coaxial transmission line $\tau = 1.51$ ns. The model triggers the 30 stages sequentially at 1.51-ns intervals; the first stage triggered is at the far left of Fig. 3.

The circuit model assumes the IMG's internal coaxial transmission line is filled with a synthetic-ester-based dielectric fluid [51]. The model makes the simplifying assumption that for frequencies of interest, the relative permittivity of the fluid has a constant value of 3.2 [51].

We define E_{IMG} to be the total electrical energy initially stored by the IMG capacitors:

$$E_{\text{IMG}} = \frac{1}{2} n_s C_s V_s^2, \tag{7}$$

$$C_s = n_b C_b = n_b \left(\frac{C}{2}\right), \tag{8}$$

$$V_s = V_b. \tag{9}$$

The quantity n_s is the total number of IMG stages, C_s is the capacitance of each stage, V_s is the initial charge voltage across each stage, n_b is the total number of bricks per stage, C_b is the capacitance of each brick, C is the capacitance of each capacitor, and V_b is the initial charge voltage across each brick. We assume the following:

$$n_s = 30, \tag{10}$$

$$n_b = 2, \tag{11}$$

$$V_b = 200\ \text{kV}. \tag{12}$$

The initial electrical energy E_{IMG} stored by the IMG capacitors is 95.9 kJ. Of this, 97% is delivered to the IMG's resistive load (within 600 ns after the two switches in the first stage are triggered), and 3% is dissipated by the IMG-switch resistances.

The time history of the electromagnetic power delivered by the IMG to its load is plotted by Fig. 4. The peak load power is 458 GW, and occurs approximately 170 ns after the two switches in the first stage are triggered. Since the IMG load is purely resistive, the peak load power can be calculated

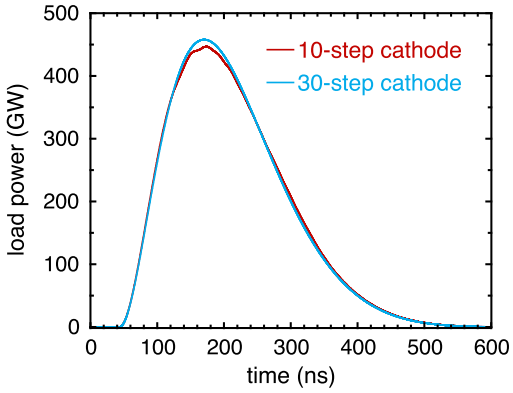


FIG. 4. Load-power time histories simulated with two 1D time-domain electromagnetic models of the 30-stage IMG. One model assumes the IMG's internal coaxial transmission line has a 10-step inner (cathode) conductor; the other, a 30-step cathode. The peak load powers calculated by the two models are 447 and 458 GW, respectively.

as $I^2 Z_{\text{load}}$ or V^2/Z_{load}, where I and V are the peak load current and voltage, respectively. (The load power is calculated in the same manner for all the 0D, 1D, 2D, and 3D simulations described by the article, since all the simulations assume the load impedance is purely resistive.) The 10%–90% rise time of the load power is 126 ns.

We also considered a 30-stage IMG with a 10-step cathode, since such a cathode may be less expensive to fabricate than a 30-step design. The 10-step cathode has one step for every three IMG stages; the impedance of each of the 10 steps is assumed to be as follows:

$$Z_j = jZ_1 \quad \text{for } j = 1, 2, \ldots, 10, \tag{13}$$

where

$$Z_1 = 3.3514\ \Omega. \tag{14}$$

As for the IMG with a 30-step cathode, the model of the IMG with a 10-step cathode assumes the load is a pure resistance Z_{load}:

$$Z_{10} = Z_{\text{load}} = 33.514\ \Omega. \tag{15}$$

The time history of the load power for the IMG with a 10-step cathode is plotted by Fig. 4. The peak load powers achieved by the 10-step and 30-step cathodes are 447 and 458 GW, respectively. Hence reducing the number of cathode steps from 30 to 10 reduces the peak load power by 2.4%. We also observe that near the time of peak power, the shape of the power time history for the 10-step configuration differs slightly from that obtained with 30 steps, which is due to stage-to-stage impedance mismatches of the 10-step design.

The numerical energy-conservation errors of the 10- and 30-step simulations conducted with the CHICAGO-CIRCUITS code are both less than 0.01%. The results plotted by Fig. 4 are consistent with those obtained with the SCREAMER circuit code [52–54].

III. 2D ELECTROMAGNETIC MODELS

We have developed two 2D (r, z) finite-difference time-domain electromagnetic models of the IMG illustrated by Fig. 2. One model assumes the IMG's internal coaxial transmission line has a 10-step cathode; the other, a 30-step cathode.

The two models are represented by Fig. 5. The 2D simulations are driven radially by 30 inlet boundaries. Each boundary is connected to a transmission-line-circuit model of two bricks connected electrically in parallel. The 30 identical circuit models are developed with the CHICAGO-CIRCUITS code [49]; the circuit parameters are consistent with those used for the simulations summarized by Sec. II. Each of the 30 circuits is triggered using the method described by Sec. II.

As indicated by Fig. 5, the 2D finite-difference region of each of the two IMGs has an outer radius of 20 cm; the regions are modeled with CHICAGO, a finite-difference time-domain electromagnetic particle-in-cell code [50].

Figure 5 plots the energy density within the electromagnetic-simulation volumes at 170 ns, near the time of peak load power. The simulations use an explicit electromagnetic-field solution with radial spatial resolution $\Delta r = 2$ mm and axial spatial resolution $\Delta z = 2.5$ mm. The inner radius of the outer (anode) conductor of the IMG's internal coaxial transmission line is 20 cm. The actual values of Z_j

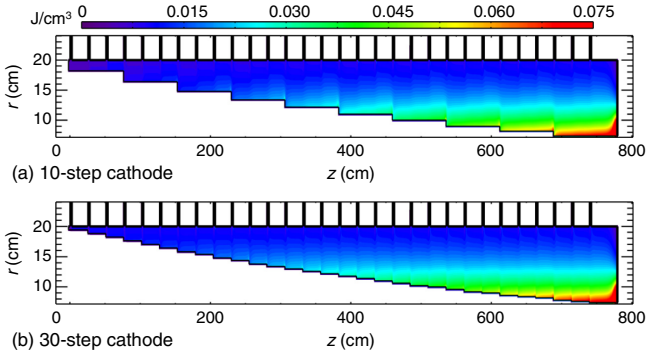


FIG. 5. (a) Electromagnetic-field-energy density within the 30-stage IMG as calculated by a 2D finite-difference time-domain electromagnetic simulation. The internal coaxial transmission line of the IMG has a 10-step inner (cathode) conductor. (b) Energy density for an IMG with a 30-step cathode. Both energy densities are those near peak load power. The 2D simulation regions extend from $z = 0$ to $z = 770$ cm, and from $r = 7.4$ cm to $r = 20$ cm. The simulations are driven radially by 30 inlet boundaries. Each boundary is connected to a transmission-line-circuit model of two IMG bricks connected electrically in parallel.

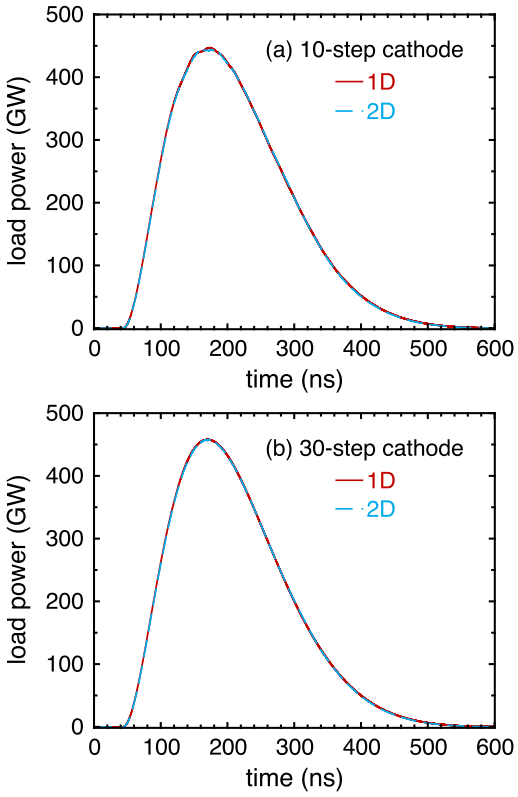


FIG. 6. (a) Load-power time histories simulated with the 1D and 2D time-domain electromagnetic models of the 30-stage IMG with a 10-step cathode. (b) Load-power time histories for the IMG with a 30-step cathode. The peak 1D and 2D powers calculated with the 10-step cathode are 447 and 444 GW, respectively; the peak 1D and 2D powers calculated with the 30-step cathode are both 458 GW.

for each stage are constrained by the radial-grid spacing and are therefore only approximately given by Eqs. (4)–(6) and Eqs. (13)–(15).

The 2D simulations find that for the 10-step- and 30-step cathodes, the peak powers delivered to the resistive load are 444 and 458 GW, respectively. The 1D and 2D simulations agree to within 1%. The 1D and 2D load-power time histories are plotted by Fig. 6. The minor discrepancies between the peak load powers of the 1D and 2D models are likely due to nonideal boundary conditions between the brick circuits and 2D finite-difference grid used for the simulations conducted within $r = 20$ cm. Section II observes that for the 1D simulations, the load-power time history near the time of peak power obtained with the 10-step cathode differs slightly from that obtained with the 30-step cathode; this result is confirmed by the 2D simulations.

The numerical energy-conservation errors of the 10-step and 30-step 2D simulations are both less than 0.3%.

IV. 3D ELECTROMAGNETIC MODEL

We have developed a 3D (r, θ, z) finite-difference time-domain electromagnetic model of the 30-stage IMG. The

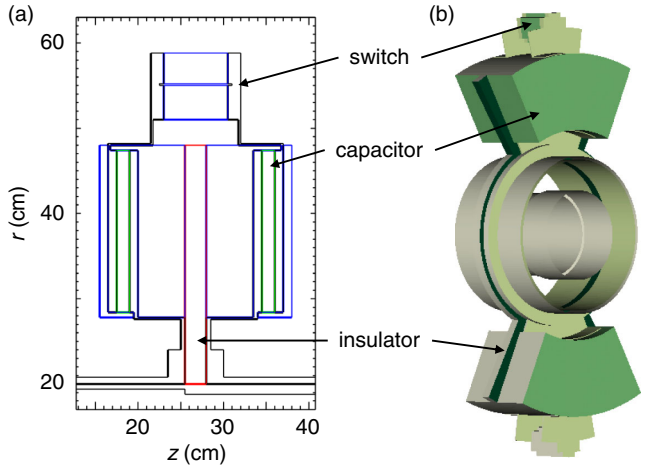


FIG. 7. 3D model of a single stage of the 30-stage IMG. Each stage is powered by two bricks located 180° apart. (a) Cross-sectional view of the stage; (b) illustration of the bricks.

3D model was developed with the CHICAGO code [50]. The model was constructed with radial spatial resolution $\Delta r = 2$ mm, azimuthal angular resolution $\Delta\theta = 0.035$ radians, and axial spatial resolution $\Delta z = 2.5$ mm.

The 3D model is not powered by external transmission-line circuits that represent the 60 bricks; instead, the model includes a 3D finite-difference time-domain electromagnetic model of each brick. (Reference [44] describes a 3D (r, θ, z) electromagnetic model of a linear transformer driver that is also powered by 3D brick models.)

As indicated by the previous sections, a single stage of the 30-stage IMG is powered by two bricks connected electrically in parallel. As suggested by Fig. 7, the bricks are attached 180° apart to two adjacent segments of the outer (anode) conductor of the IMG's coaxial transmission line. The two anode segments consist of two hollow cylindrical conductors separated by a gap filled with a dielectric spacer. The IMG bricks generate a power pulse that flows through the gap between the two anode segments, and into the IMG's centrally located coaxial transmission line.

Each brick model includes 3D representations of the two capacitors, the switch (which includes a current-carrying channel that has a time-dependent resistance), and connecting hardware that gives the desired brick inductance.

The model assumes the entire 30-stage IMG is immersed in a synthetic-ester-based dielectric liquid with relative permittivity $\varepsilon_r = 3.2$ [51]. Conducting walls are located at the upstream and downstream ends of the 3D simulation volume; the walls are located 200 cm away from the upstream and downstream ends of the IMG, respectively. A radial outgoing-wave boundary is located at $r = 120$ cm to allow electromagnetic power radiated by the bricks to escape the simulation volume. A series of conducting vanes, which extend radially from $r = 100$ cm to $r = 120$ cm and are spaced 25.5 cm apart axially, assist in channeling radiated energy away from the IMG in a numerically stable way.

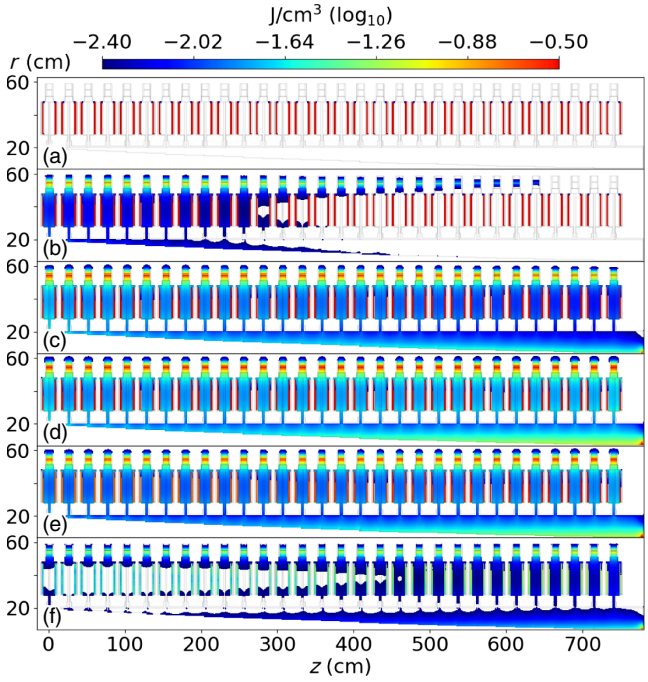


FIG. 8. Cross-sectional view of the time-dependent electromagnetic-field-energy density within the 30-stage IMG. The IMG's internal coaxial transmission line has a 30-step inner (cathode) conductor. The view illustrated here represents the plane that bisects the bricks. The energy density is calculated by a 3D finite-difference time-domain electromagnetic simulation. (a) At $t = 0$, none of the IMG's 60 switches has triggered; all the electrical energy is still within the IMG's energy-storage capacitors. (b) At $t = 45$ ns, all the switches have triggered, and energy begins to flow from the capacitors to the IMG's coaxial transmission line. (c) At $t = 90$ ns, electrical power at the load is increasing. (d) At $t = 180$ ns, electrical power at the load is near its peak value. (e) At $t = 225$ ns, the load power is decreasing, and the energy within the capacitors has been substantially depleted. (f) At $t = 326$ ns, the load power is less than half its peak value.

At the start of a 3D electromagnetic simulation, a Poisson solution is obtained to initialize the electric field within the capacitors. The stored electrical energy within the two capacitors of a brick is discharged when the brick's switch is triggered; i.e., when the resistance of the switch's current-carrying channel drops from an initially high value to a much lower final one.

The IMG stages are triggered sequentially at 1.51-ns intervals, as outlined by Sec. II. Electromagnetic power flows from the bricks to the IMG's centrally located coaxial transmission line, which in turn delivers the power to the resistive load. Figure 8 illustrates the distribution of energy within the IMG at six different times, and the transfer of electrical energy from the capacitors to the load. [Figure 8 does not include the upstream and downstream conducting walls, and radial outgoing-wave boundary (with conducting vanes), that are used by the numerical simulation.]

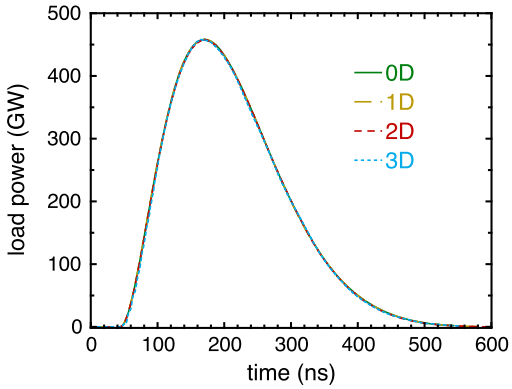


FIG. 9. Load-power time histories simulated with the 0D, 1D, 2D, and 3D models of the 30-stage IMG with a 30-step cathode. For each of the four simulations, the peak load power is 458 GW (to three significant figures). Such agreement must be considered fortuitous; numerical-error and radiation-loss estimates suggest the peak powers could differ by as much as ∼1%.

The 3D simulation finds that when the cathode has 30 steps, the peak power delivered by the 30-stage IMG to its resistive load is 458 GW. The 1D and 2D simulations also find the 30-step cathode delivers a peak load power of 458 GW. The three peak load powers agree to within less than 1%. Load-power time histories for the 1D, 2D, and 3D simulations are plotted by Fig. 9.

The 1D and 2D models of the IMG do not allow for electromagnetic energy to be radiated away from the IMG. The 3D model allows for energy to be radiated by the bricks, as well as the axial gaps between adjacent segments of the IMG's outer conductor. The 3D model simulates the emission of electromagnetic radiation due to currents flowing on surfaces of the IMG conductors. (The model does not simulate visible, x-ray, or bremsstrahlung emission from charged particles within the IMG switches. The energy lost within a switch is modeled simply as a component of the series brick resistance.)

The 3D simulation suggests the total energy that escapes the simulation volume (over a time interval of 600 ns after the first stage is triggered) is ∼1 kJ, or ∼1% of the energy initially stored by the IMG capacitors. The energy that radiates from the gaps between adjacent anode segments is ∼0.2 kJ (∼0.2%); therefore, the energy radiated by the bricks is ∼0.8 kJ (∼0.8%).

Figure 9 and the peak load powers given above suggest radiated losses reduce the peak load power by less than ∼1%. The numerical energy-conservation error of the 3D simulation is less than 0.3%.

V. OPTIMUM LOAD IMPEDANCE

The simulations described by this article assume the IMG load is an ideal purely resistive circuit element with a 33.514-Ω impedance. This is 34% above that required to

maximize the peak load power. This section outlines motivations for overmatching the load impedance.

The peak power delivered by an IMG to a purely resistive load is maximized when the load impedance Z_{load} is equal to Z_{power}, which is defined by the following expression [3,34,36]:

$$Z_{\text{power}} = 1.1\sqrt{\frac{L_{\text{IMG}}}{C_{\text{IMG}}}} + 0.8\ R_{\text{IMG}}, \tag{16}$$

where

$$L_{\text{IMG}} = \frac{n_s L_b}{n_b} = \frac{2n_s L}{n_b}, \tag{17}$$

$$C_{\text{IMG}} = \frac{n_b C_b}{n_s} = \frac{n_b C}{2n_s}, \tag{18}$$

$$R_{\text{IMG}} = \frac{n_s R_b}{n_b} = \frac{2n_s R}{n_b}. \tag{19}$$

The quantity L_{IMG} is the series inductance of the IMG, C_{IMG} is the series capacitance of the IMG, R_{IMG} is the series resistance (not including Z_{load}) of the IMG, n_s is the number of IMG stages, and n_b is the number of bricks per stage. The quantities L_b, C_b, and R_b [which are defined by Eqs. (17)–(19)] are the series inductance, capacitance, and resistance, respectively, of a single IMG brick.

We have assumed the 30-stage IMG considered by this article has the circuit parameters listed by Eqs. (1)–(3), (10), and (11); hence

$$L_{\text{IMG}} = 2.58\ \mu\text{H}, \tag{20}$$

$$C_{\text{IMG}} = 5.33\ \text{nF}, \tag{21}$$

$$R_{\text{IMG}} = 1.05\ \Omega. \tag{22}$$

According to Eq. (16), the peak power delivered by such an IMG to a resistive load is maximized when the load impedance $Z_{\text{load}} = Z_{\text{power}} = 25.0\ \Omega$.

Figure 10 plots the normalized peak load power as a function of the normalized load impedance. As indicated by the figure, there is a broad maximum in the peak power around $Z_{\text{load}}/Z_{\text{power}} = 1$.

Of course, the peak load power is not the only electrical performance parameter of interest. As indicated by Eqs. (6) and (15), the simulations described by this article assume

$$Z_{\text{load}} = 33.514\ \Omega, \tag{23}$$

which is 34% above that given by Eq. (16).

As indicated by Figs. 10 and 11, the higher load impedance reduces the peak load power by 2%, but also does the following: (i) decreases the 0%–100% rise time of the load power by 7%; (ii) decreases the peak current carried by each IMG capacitor by 15%, which decreases peak magnetic pressures and ohmic-power dissipation within the IMG capacitors and switches by 27%;

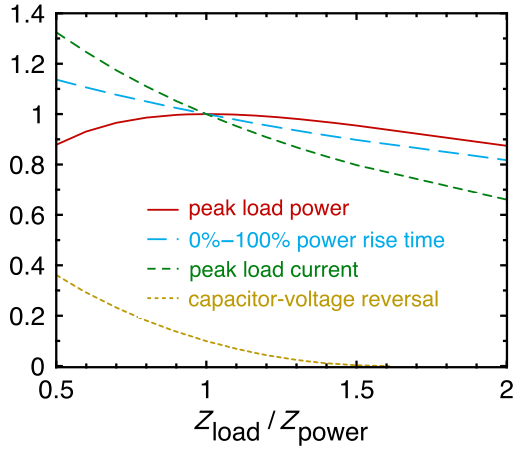


FIG. 10. Normalized peak-load power, normalized 0%–100% load-power rise time, normalized peak-load current, and capacitor-voltage reversal as functions of $Z_{\text{load}}/Z_{\text{power}}$. The quantity Z_{power} is the load impedance at which peak load power is maximized. The normalized power is the ratio of the power to that achieved when $Z_{\text{load}} = Z_{\text{power}}$; the other two normalized quantities are similarly defined. The plots are applicable to IMGs with the following brick parameters: $R = \alpha(0.035\ \Omega)$, $L = \alpha(86\ \text{nH})$, and $C = (159.9\ \text{nF})/\alpha$, where α is a constant.

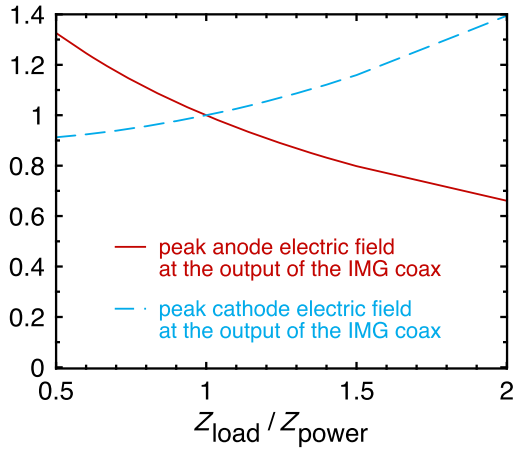


FIG. 11. Normalized peak anode electric field throughout an IMG's centrally located coaxial transmission line, and normalized peak cathode electric field at the output of the IMG's coaxial line, as functions of $Z_{\text{load}}/Z_{\text{power}}$. The quantity Z_{power} is the load impedance at which peak load power is maximized. Each of the two normalized quantities is the ratio of the electric field to that achieved when $Z_{\text{load}} = Z_{\text{power}}$. The plot of the normalized anode field is applicable to IMGs with the following brick parameters: $R = \alpha(0.035\ \Omega)$, $L = \alpha(86\ \text{nH})$, and $C = (159.9\ \text{nF})/\alpha$, where α is a constant. The plot of the normalized cathode field is most applicable for such IMGs when $\alpha = 1$.

(iii) reduces voltage reversal at the IMG capacitors from 10% to 2%; and (4) decreases the peak electric field at the anode of the IMG's internal coaxial transmission line by 15%. As indicated by Fig. 11, the peak cathode electric field increases by 10%, but dielectric failure in a liquid insulator usually initiates at the anode.

In addition, we observe that when an IMG is used to drive a transmission-line impedance transformer, the output impedance of the IMG is typically matched to the input impedance of the transformer [26,34,35,47,55]. It is clear that the interface impedance should be chosen to maximize the efficiency of the *coupled IMG-transformer system*. The optimum interface impedance will likely be higher than that required to optimize the peak output power of just the IMG itself.

We note that when $R_{\mathrm{IMG}} \ll (L_{\mathrm{IMG}}/C_{\mathrm{IMG}})^{1/2}$, an IMG is critically damped when $Z_{\mathrm{load}} = 2(L_{\mathrm{IMG}}/C_{\mathrm{IMG}})^{1/2} = 1.8Z_{\mathrm{power}}$. Under such conditions, there is no voltage reversal at the capacitors.

VI. SUMMARY AND DISCUSSION

Sections II, III, and IV describe 1D, 2D, and 3D time-domain electromagnetic models of an idealized coaxial 30-stage IMG, respectively. The Appendix describes a 0D circuit model of the IMG. Simulations conducted with the models demonstrate dimensionality does not significantly affect the electrical power delivered by the IMG to its load: as indicated by Fig. 9, peak load powers estimated by the 0D, 1D, 2D, and 3D simulations agree to within 1%. The 3D calculation suggests the total electromagnetic energy radiated by the bricks, and axial gaps between adjacent segments of the IMG's outer conductor, reduces the peak load power by less than ∼1%.

The 1D simulations described by Sec. II used a single processor of an average desktop computer, and executed in less than a few seconds with a computational time step of 5×10^{-3} ns. The 2D simulations described by Sec. III used 160 processor cores on high-performance computing nodes, and executed in less than 4 min with a time step of 4.7×10^{-3} ns. The 3D simulation described by Sec. IV used 600 processor cores, and executed in 150 h with a time step of 4×10^{-3} ns. (We observe that the 3D simulation could be executed efficiently on a larger number of cores to reduce computational time.)

The results of this study demonstrate that the electrical performance of an *idealized* IMG is well described by a detailed transmission-line-circuit simulation, which is far less computationally intensive—and orders-of-magnitude faster—than equivalent 2D and 3D finite-difference time-domain electromagnetic simulations. However, 2D simulations provide useful checks on the electrical performance of inner-conductor designs; 3D simulations provide estimates of the electromagnetic power radiated by an IMG.

It is clear that the 0D, 1D, 2D, and 3D models outlined by this article could be adapted to assess computationally competing IMG designs, and conduct a variety of numerical IMG experiments, *before* an IMG is constructed. In addition, the models could be extended to include the switch-triggering circuit, the capacitor-charging circuit, external conducting boundaries, and reactive components of the load. Furthermore, it is important to note that investigations into the packing of multiple IMGs in close proximity within an oil-containment tank could be conducted with 3D simulations. These would inform the design of an IMG-based prime-power system of a pulsed-power accelerator, such as that illustrated by Fig. 1.

ACKNOWLEDGMENTS

The authors are immensely grateful to the following colleagues for critical discussions and sustained support: Farhat Beg, Dan Behne, Mike Campbell, Dustin Cannon, Amanda Cuttler, Rebecca Dylla-Spears, Lee Ellison, Anson Grover, Ken Heinz, Randy Hicks, Brian Hutsel, Dan Jobe, Kirk Keilholtz, Patrick Knapp, Ray Leeper, Mike Mazarakis, Ryan McBride, Harry McLean, Donn McMahon, Robin Miles, Rick Olson, Noah Pflueger-Peters, Ashton Ray, Will Regan, Ignacio Rodriguez, Steve Sampayan, Mark Savage, Paul Schmit, Ralph Schneider, Jens Schwarz, Rob Sharpe, Bryan Sims, Anup Singh, and Don Voss. The authors are also immensely indebted to our many other colleagues at the following organizations for invaluable contributions: Voss Scientific, Pacific Fusion, Lawrence Livermore National Laboratory, R. E. Beverly III and Associates, CSI Technologies, General Atomics Energy Group, Laboratory of Laser Energetics at the University of Rochester, Mission Support and Test Services, MuEpsln, National Nuclear Security Administration, and Sandia National Laboratories. The work was performed under the auspices of the U.S. Department of Energy by Lawrence Livermore National Laboratory under Contract No. DE-AC52-07NA27344.

APPENDIX: 0D CIRCUIT MODEL

We have developed a 0D circuit model of the 30-stage IMG with a 30-step cathode. The model was constructed with the SCREAMER circuit code [52–54]. The model assumes the IMG switches are triggered sequentially, as described by Sec. II.

Such an IMG can be modeled as a single simple *LCR* circuit that drives a resistive load [3]. The single-loop four-element circuit is illustrated by Fig. 12. The circuit elements L_{IMG}, C_{IMG}, and R_{IMG} are given by Eqs. (20), (21), and (22), respectively; the load impedance Z_{load} is given by Eq. (23).

The time history of the electrical power delivered to the load as determined with the 0D model is obtained with a

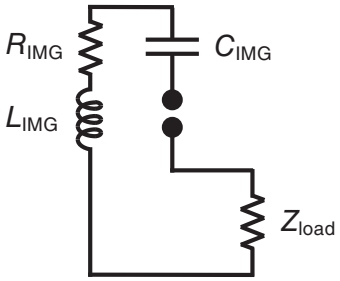


FIG. 12. 0D single-loop four-element circuit model of an IMG. The model is applicable when the number of IMG stages equals the number of steps in the inner conductor of the IMG's internal coaxial transmission line, and the IMG switches are triggered sequentially as described by Sec. II. The quantity $L_{IMG} = (n_s L_b)/n_b$, $C_{IMG} = (n_b C_b)/n_s$, and $R_{IMG} = (n_s R_b)/n_b$, where n_s is the number of IMG stages and n_b is the number of IMG bricks per stage. The quantities L_b, C_b, and R_b are the series inductance, capacitance, and resistance of a single IMG brick, respectively. For the 30-step IMG considered by this article, $L_{IMG} = 2.58$ μH, $C_{IMG} = 5.33$ nF, $R_{IMG} = 1.05$ Ω, and $Z_{load} = 33.514$ Ω. The load-power time history simulated with the 0D model is plotted by Fig. 9.

SCREAMER circuit simulation and plotted by Fig. 9. As indicated by the figure, the time history agrees with those obtained with the 1D, 2D, and 3D models. The peak load power calculated with the 0D model is 458 GW, which is the same (to three significant figures) as those calculated with the 1D, 2D, and 3D models. (An analytic solution to the *LCR* circuit equations gives 458 GW as well.)

The 0D SCREAMER simulation was conducted with a single processor of an average desktop computer, and executed in 0.012 s with a computational time step of 5×10^{-2} ns. The energy conservation error is less than 0.01%.

[1] E. Marx, Versuche über die Prüfung von Isolatoren mit Spannungsstößen (Experiments on the Testing of Insulators using High Voltage Pulses), Elektrotech. Z **45**, 652 (1924).

[2] T. H. Martin, The Hydra electron beam accelerator, IEEE Trans. Nucl. Sci. **20**, 289 (1973).

[3] W. A. Stygar, K. R. LeChien, M. G. Mazarakis, M. E. Savage, B. S. Stoltzfus, K. N. Austin, E. W. Breden, M. E. Cuneo, B. T. Hutsel, S. A. Lewis, G. R. McKee, J. K. Moore, T. D. Mulville, D. J. Muron, D. B. Reisman, M. E. Sceiford, and M. L. Wisher, Impedance-matched Marx generators, Phys. Rev. Accel. Beams **20**, 040402 (2017).

[4] R. D. McBride, W. A. Stygar, M. E Cuneo *et al.*, A primer on pulsed power and linear transformer drivers for high energy density physics applications, IEEE Trans. Plasma Sci. **46**, 3928 (2018).

[5] T. Huiskamp and J. J. van Oorschot, Fast pulsed power generation with a solid-state impedance-matched Marx generator: Concept, design, and first implementation, IEEE Trans. Plasma Sci. **47**, 4350 (2019).

[6] M. Azizi, J. J. van Oorschot, and T. Huiskamp, Ultrafast switching of SiC MOSFETs for high-voltage pulsed-power circuits, IEEE Trans. Plasma Sci. **48**, 4262 (2020).

[7] Brendan Sporer, Nicholas M. Jordan, and Ryan McBride, Testing of the prototype BLUE linear transformer driver (LTD) cavity at University of Michigan, in *Proceedings of the 2020 IEEE International Conference on Plasma Science, Singapore* (IEEE, Piscataway, NJ, 2020).

[8] P.-A. Gourdain, M. Evans, P. Efthimion, R. Ellis, W. Fox, H. R. Hasson, H. Ji, R. V. Shapovalov, J. R. Young, and I. West-Abdallah, Coreless fast pulsed-power drivers, IEEE Trans. Plasma Sci. **49**, 2161 (2021).

[9] B. Guegan, F. Bayol, D. Arnal, and Patrick Mouly, Megavolt impedance-matched Marx, in *Proceedings of the 2021 IEEE Pulsed Power Conference, Denver, CO* (IEEE, Piscataway, NJ, 2021).

[10] K. R. LeChien, W. A. Stygar, M. G. Anderson, D. A. Max, R. M. Anaya, C. B. Beatty, A. D. White, J. J. Trueblood, A. M. Benson, R. E. Beverly, R. S. Chaffee, J. E. Cortes, W. A. Drews, R. K. Hicks, F. A. Howland, D. B. Norton, R. D. Speer, and J. A. Watson, *Sirius I: prototype of a prime-power source for future 1–10 GJ fusion-yield experiments*, Lawrence Livermore National Laboratory Report No. LLNL-TR-846570 (2023).

[11] J. J. van Oorschot and T. Huiskamp, Fast and flexible, arbitrary waveform, 20-kV, solid-state, impedance-matched Marx generator, IEEE Trans. Plasma Sci. **51**, 560 (2023).

[12] J. J. van Oorschot and T. Huiskamp, Rogowski and D-dot sensors for nanosecond high-voltage and high-current pulse measurements in impedance-matched pulse generators, IEEE Trans. Plasma Sci. **51**, 1107 (2023).

[13] M. G. Anderson, K. R. LeChien, W. A. Stygar *et al.*, Sirius I prototype: A prime-power source for future 1–10 GJ fusion-yield experiments, in *Proceedings of the 2023 IEEE Pulsed Power Conference, San Antonio, TX* (IEEE, Piscataway, NJ, 2023).

[14] T. Huiskamp, M. Azizi, C. Ton, and J. van Oorschot, Pulsed streamer discharge generation in a wire-cylinder arrangement with 30-kV, nanosecond, arbitrary waveform pulses, in *Proceedings of the 2023 IEEE International Conference on Plasma Science, Santa Fe, NM* (IEEE, Piscataway, NJ, 2023).

[15] J. Leckbee, T. Awe, M. Cuneo, R. Curry *et al.*, Pulsed power science and technology development at various scales at Sandia National Laboratories, in *Proceedings of the 2023 IEEE Pulsed Power Conference, San Antonio, TX* (IEEE, Piscataway, NJ, 2023).

[16] J. J. van Oorschot and T. Huiskamp, Impact of impedance-matching on internal reflections and output pulse shape in impedance-matched pulse generators, in *Proceedings of the 2023 IEEE Pulsed Power Conference, San Antonio, TX* (IEEE, Piscataway, NJ, 2023).

[17] M. Feizi, B. Vermulst, and T. Huiskamp, Ultra-fast switching of GaN transistors for nanosecond-pulse generation using GaN HEMTs-based drivers, in *Proceedings of the 13th International Conference on Power Electronics, Machines and Drives, Nottingham, UK* (IEEE, Piscataway, NJ, 2024).

[18] H. Zhang, Z. Zhang, and H. Yang, Research on the impedance-matched Marx generator for pulsed power application, in *Proceedings of the 2024 IEEE International Conference on Plasma Science, Beijing* (IEEE, Piscataway, NJ, 2024).

[19] Vahid Damideh *et al.*, Experimental results of a 330 GW impedance-matched Marx generator, Sci. Rep. **14**, 16889 (2024).

[20] C. Leland Ellison, Vincent Garcia, Matthew Gomez, Gary P. Grim, Jim H. Hammer, Christopher A. Jennings, Patrick Knapp, Keith R. LeChien, Nathan Meezan, Robert Peterson, Adam Reyes, Adam Steiner, William A. Stygar, Petros Tzeferacos, Dale Welch, and Alex Zylstra, Opportunities in pulsed magnetic fusion energy, arXiv:2408.15206.

[21] W. Stygar, R. Focia, W. Fowler, B. Hutsel, M. Mazarakis, J. Porter, S. Roznowski, M. Savage, and B. Stoltzfus, Conceptual design of a megabar-class accelerator for material-physics experiments, in *Proceedings of the Fourth Fundamental Science with Pulsed Power Workshop: Research Opportunities and User Meeting* (Sandia National Laboratories, Albuquerque, NM, 2012).

[22] B. S. Stoltzfus, K. Austin, B. T. Hutsel, D. Reisman, M. E. Savage, and W. A. Stygar, Variable-pulse-shape pulsed-power accelerator, U.S. Patent Application US 2015/0366045 A1, 2015.

[23] D. B. Reisman, B. S. Stoltzfus, W. A. Stygar, K. N. Austin, E. M. Waisman, R. J. Hickman, J.-P. Davis, T. A. Haill, M. D. Knudson, C. T. Seagle, J. L. Brown, D. A. Goerz, R. B. Spielman, J. A. Goldlust, and W. R. Cravey, Pulsed power accelerator for material physics experiments, Phys. Rev. ST Accel. Beams **18**, 090401 (2015).

[24] E. M. Waisman, D. B. Reisman, B. S. Stoltzfus, W. A. Stygar, M. E. Cuneo, T. A. Haill, J.-P. Davis, J. L. Brown, C. T. Seagle, and R. B. Spielman, Optimization of current waveform tailoring for magnetically-driven isentropic compression experiments, Rev. Sci. Instrum. **87**, 063906 (2016).

[25] W. A. Stygar *et al.*, Conceptual design of a 10^{13}-W pulsed-power accelerator for megajoule-class dynamic material-physics experiments, Phys. Rev. Accel. Beams **19**, 070401 (2016).

[26] W. Stygar *et al.*, Conceptual design of a 960-TW accelerator powered by impedance-matched Marx generators, in *Proceedings of the 21st IEEE International Pulsed Power Conference, Brighton, UK* (IEEE, Piscataway, NJ, 2017).

[27] B. M. Koval'chuk, V. A. Vizir', A. A. Kim, E. V. Kumpyak, S. V. Loginov, A. N. Bastrikov, V. V. Chervyakov, N. V. Tsoi, P. Monjaux, and D. Kh'yui, Fast primary storage device utilizing a linear pulse transformer, Russ. Phys. J. **40**, 1142 (1997).

[28] A. N. Bastrikov, V. A. Vizir, S. N. Volkov, V. G. Durakov, A. M. Efremov, V. B. Zorin, A. A. Kim, B. M. Kovalchuk, E. V. Kumpjak, S. V. Loginov, V. A. Sinebryuhov, N. V. Tsou, V. V. Cervjakov, V. P. Yakovlev, and G. A. Meyats, Primary energy storages based on linear transformer stages, Lasers Part. Beams **21**, 295 (2003).

[29] M. E. Savage, Balanced two-capacitor brick for linear transformer drivers (unpublished).

[30] I. D. Smith, Induction voltage adders and the induction accelerator family, Phys. Rev. ST Accel. Beams **7**, 064801 (2004).

[31] C. L. Olson, Z-pinch inertial fusion energy, in *Landholt-Börnstein Handbook on Energy Technologies*, edited by W. Martienssen, and K. Heinloth, Vol. VIII/3 of (Springer-Verlag, Berlin, 2005).

[32] J. J. Leckbee, J. E. Maenchen, D. L. Johnson, S. Portillo, D. M. Van De Valde, D. V. Rose, and B. V. Oliver, Design, simulation, and fault analysis of a 6.5-MV LTD for flash x-ray radiography, IEEE Trans. Plasma Sci. **34**, 1888 (2006).

[33] D. V. Rose, D. R. Welch, B. V. Oliver, J. J. Leckbee, J. E. Maenchen, D. L. Johnson, A. A. Kim, B. M. Kovalchuk, and V. A. Sinebryukhov, Numerical analysis of a pulsed compact LTD system for electron beam-driven radiography, IEEE Trans. Plasma Sci. **34**, 1879 (2006).

[34] W. A. Stygar, M. E. Cuneo, D. I. Headley, H. C. Ives, R. J. Leeper, M. G. Mazarakis, C. L. Olson, J. L. Porter, T. C. Wagoner, and J. R. Woodworth, Architecture of Petawatt-class z-pinch accelerators, Phys. Rev. ST Accel. Beams **10**, 030401 (2007).

[35] D. R. Welch, T. C. Genoni, D. V. Rose, N. L. Bruner, and W. A. Stygar, Optimized transmission-line impedance transformers for petawatt-class pulsed-power accelerators, Phys. Rev. ST Accel. Beams **11**, 030401 (2008).

[36] W. A. Stygar, W. E. Fowler, K. R. LeChien, F. W. Long, M. G. Mazarakis, G. R. McKee, J. L. McKenney, J. L. Porter, M. E. Savage, B. S. Stoltzfus, D. M. Van De Valde, and J. R. Woodworth, Shaping the output pulse of a linear-transformer-driver module, Phys. Rev. ST Accel. Beams **12**, 030402 (2009).

[37] M. G. Mazarakis, W. E. Fowler, A. A. Kim, V. A. Sinebryukhov, S. T. Rogowski, R. A. Sharpe, D. H. McDaniel, C. L. Olson, J. L. Porter, K. W. Struve, W. A. Stygar, and J. R. Woodworth, High current, 0.5-MA, fast, 100-ns, linear transformer driver experiments, Phys. Rev. ST Accel. Beams **12**, 050401 (2009).

[38] A. A. Kim, M. G. Mazarakis, V. A. Sinebryukhov, B. M. Kovalchuk, V. A. Visir, S. N. Volkov, F. Bayol, A. N. Bastrikov, V. G. Durakov, S. V. Frolov, V. M. Alexeenko, D. H. McDaniel, W. E. Fowler, K. LeChien, C. Olson, W. A. Stygar, K. W. Struve, J. Porter, and R. M. Gilgenbach, Development and tests of fast 1-MA linear transformer driver stages, Phys. Rev. ST Accel. Beams **12**, 050402 (2009).

[39] J. R. Woodworth, J. A. Alexander, F. R. Gruner, W. A. Stygar, M. J. Harden, J. R. Blickem, G. J. Dension, F. E. White, L. M. Lucero, H. D. Anderson, L. F. Bennett, S. F. Glover, D. Van De Valde, and M. G. Mazarakis, Low-inductance gas switches for linear transformer drivers, Phys. Rev. ST Accel. Beams **12**, 060401 (2009).

[40] K. LeChien *et al.*, A 1-MV, 1-MA, 0.1-Hz linear transformer driver utilizing an internal water transmission line, in *Proceedings of the 17th IEEE International Pulsed Power Conference* (IEEE, Piscataway, NJ, 2009), p. 1186.

[41] M. G. Mazarakis *et al.*, High-current linear transformer driver development at Sandia National Laboratories, IEEE Trans. Plasma Sci. **38**, 704 (2010).

[42] A. A. Kim, M. G. Mazarakis, V. I. Manylov, V. A. Vizir, and W. A. Stygar, Energy loss due to eddy current in linear

transformer driver cores, Phys. Rev. ST Accel. Beams **13**, 070401 (2010).

[43] J. R. Woodworth, W. A. Stygar, L. F. Bennett, M. G. Mazarakis, H. D. Anderson, M. J. Harden, J. R. Blickem, F. R. Gruner, and R. White, New low inductance gas switches for linear transformer drivers, Phys. Rev. ST Accel. Beams **13**, 080401 (2010).

[44] D. V. Rose, C. L. Miller, D. R. Welch, R. E. Clark, E. A. Madrid, and C. B. Mostrom, W. A. Stygar, K. R. LeChien, M. A. Mazarakis, W. L. Langston, J. L. Porter, and J. R. Woodworth, Circuit models and three-dimensional electromagnetic simulations of a 1-MA linear transformer driver stage, Phys. Rev. ST Accel. Beams **13**, 090401 (2010).

[45] J. R. Woodworth, W. E. Fowler, B. S. Stoltzfus, W. A. Stygar, M. E. Sceiford, M. G. Mazarakis, H. D. Anderson, M. J. Harden, J. R. Blickem, R. White, and A. A. Kim, Compact 810 kA linear transformer driver cavity, Phys. Rev. ST Accel. Beams **14**, 040401 (2011).

[46] T. C. Genoni, D. V. Rose, R. E. Clark, D. R. Welch, and W. A. Stygar, Efficient ferromagnetic core impedance model with application to finite-difference time-domain simulation, Phys. Rev. ST Accel. Beams **15**, 010401 (2012).

[47] W. A. Stygar *et al.*, Conceptual designs of two petawatt-class pulsed-power accelerators for high-energy-density-physics experiments, Phys. Rev. ST Accel. Beams **18**, 110401 (2015).

[48] J. D. Douglass, B. T. Hutsel, J. J. Leckbee, T. D. Mulville *et al.*, 100 GW linear transformer driver cavity: Design, simulations, and performance, Phys. Rev. Accel. Beams **21**, 120401 (2018).

[49] C. B. Mostrom, E. D. Watson, D. R. Welch, C. A. Mostrom, R. E. Clark, D. V. Rose, and A. M. Russell, Circuit-GUI User's Manual, Voss Scientific Report No. VSL-2315, 2023. CHICAGO™ is a trademark of Voss Scientific.

[50] D. R. Welch, N. Bennett, I. Paraschiv, D. V. Rose, and C. Thoma, Fast hybrid particle-in-cell technique for pulsed-power accelerators, Phys. Rev. Accel. Beams **23**, 110401 (2020). CHICAGO™ is a trademark of Voss Scientific.

[51] M&I Materials Ltd., Technical brochure, MIVOLT DFK dielectric liquid, https://mivoltcooling.com/dielectric-fluids/mivolt-dfk/.

[52] M. L. Kiefer and M. M. Widner, SCREAMER—a single-line pulsed-power design tool, in *Proceedings of the 5th IEEE International Pulsed Power Conference, Washington, DC*, edited by M. F. Rose and P. J. Turchi (IEEE, Piscataway, NJ, 1985), p. 685.

[53] R. B. Spielman, M. L. Kiefer, K. L. Shaw, K. W. Struve, and M. M. Widner, SCREAMER: A pulsed Power Design Tool, User's Guide for Version 4.4.3 (2020), https://www.isu.edu/iac/research/screamer/.

[54] R. B. Spielman and Y. Gryazin, SCREAMER V4.0—a powerful circuit analysis code, in *Proceedings of the 20th IEEE International Pulsed Power Conference, Austin, TX* (IEEE, Piscataway, NJ, 2015), p. 1.

[55] I. A. D. Lewis and F. H. Wells, *Millimicrosecond Pulse Techniques* (Pergamon Press, New York, 1959).